JCB Journal of Cell Biology

ARTICLE

Exocyst structural changes associated with activation of tethering downstream of Rho/Cdc42 GTPases

Guendalina Rossi[1*], Dante Lepore[2*], Lillian Kenner[3], Alexander B. Czuchra[2], Melissa Plooster[1], Adam Frost[3,4,5], Mary Munson[2], and Patrick Brennwald[1]

The exocyst complex plays a critical role in determining both temporal and spatial dynamics of exocytic vesicle tethering and fusion with the plasma membrane. However, the mechanism by which the exocyst functions and how it is regulated remain poorly understood. Here we describe a novel biochemical assay for the examination of exocyst function in vesicle tethering. Importantly, the assay is stimulated by gain-of-function mutations in the Exo70 component of the exocyst, selected for their ability to bypass Rho/Cdc42 activation in vivo. Single-particle electron microscopy and 3D reconstructions of negatively stained exocyst complexes reveal a structural change in the mutant exocyst that exposes a binding site for the v-SNARE. We demonstrate a v-SNARE requirement in our tethering assay and increased v-SNARE binding to exocyst gain-of-function complexes. Together, these data suggest an allosteric mechanism for activation involving a conformational change in one subunit of the complex, which is relayed through the complex to regulate its biochemical activity in vitro, as well as overall function in vivo.

Introduction

Spatial regulation of exocytosis is crucial for both intracellular and cell surface membrane identity, as well as overall cell polarity. Genetic, biochemical, and cell biological studies of membrane transport from the Golgi to the cell surface have identified several highly conserved protein families including the Rab GTPases, tethering factors, and SNARE proteins (Grosshans et al., 2006; Jahn and Fasshauer, 2012; Polgar and Fogelgren, 2018). Studies in the yeast system have demonstrated that the SNARE proteins Sec9, Sso1/2, and Snc1/2 function to fuse exocytic vesicles with the plasma membrane, while the Rab GTPase Sec4 and its dual effector proteins Sro7 and the multi-subunit exocyst complex are essential for vesicle tethering to specific sites on the plasma membrane (Wu et al., 2008; Finger et al., 1998). For both Sro7 and the exocyst complex, vesicle tethering appears to be linked to SNARE-mediated fusion by promoting the localized assembly of SNARE monomers into fusion-competent complexes at sites of polarized growth (Wu et al., 2008, Hattendorf et al., 2007, Morgera et al., 2012; Dubuke et al., 2015; Yue et al., 2017).

Sro7 and Sro77 were identified as binding partners for the target SNARE (t-SNARE) Sec9 and were shown to be essential for exocytosis at all but high temperatures (Lehman et al., 1999). Structural studies demonstrated that Sro7 is part of the Lgl/tomosyn family of dual β-propeller structures (Hattendorf et al., 2007) and that the binding site for the Sec4 GTPase lies within a conserved "cleft" formed by the intersection of the two propellers (Watson et al., 2015). Although Sro7 is not stably associated with the exocyst, it was shown to transiently interact with the Exo84 subunit of the exocyst complex (Zhang et al., 2005). Oligomerization of Sro7 monomers bound to Sec4-GTP on opposing membranes is thought to bridge vesicles to the target membrane (Rossi et al., 2018).

The exocyst is a member of the CATCHR (complexes associated with tethering containing helical rods) family of multisubunit tethering complexes required for transport from the Golgi to the plasma membrane (TerBush et al., 1996, Baker and Hughson, 2016, Lepore et al., 2018). Exocyst comprises eight subunits, Sec3, Sec5, Sec6, Sec8, Sec10, Sec15, Exo84, and Exo70

[1]Department of Cell Biology and Physiology, University of North Carolina School of Medicine, Chapel Hill, NC; [2]Department of Biochemistry and Molecular Pharmacology, University of Massachusetts Medical School, Worcester, MA; [3]Department of Biochemistry and Biophysics, University of California, San Francisco, San Francisco, CA; [4]Chan Zuckerberg Biohub, University of California, San Francisco, San Francisco, CA; [5]California Quantitative Biosciences Institute, University of California, San Francisco, San Francisco, CA.

*G. Rossi and D. Lepore contributed equally to this paper; Correspondence to Patrick Brennwald: pjbrennw@med.unc.edu; Mary Munson: mary.munson@umassmed.edu.

(TerBush et al., 1996; Guo et al., 1999b) and acts as a Rab effector through a direct interaction between vesicle bound Sec4-GTP and the Sec15 subunit of the exocyst complex (Guo et al., 1999a). Subsequently, an interaction between the Sec6 subunit of the exocyst complex and the vesicle SNARE (v-SNARE) Snc2 has suggested that the exocyst may act as a "coincidence detector" by requiring both the v-SNARE and the Rab GTPase for its association with post-Golgi vesicles (Shen et al., 2013). Interactions between the Exo70 and Sec3 subunits of the exocyst with phospholipids and GTPases at the plasma membrane are thought to allow the complex to tether vesicles to the target membrane (Zhang et al., 2008; He et al., 2007; Wu et al., 2008). In addition, the exocyst can also interact with the t-SNAREs Sec9 and Sso1 as part of its role in SNARE assembly downstream of tethering (Morgera et al., 2012; Dubuke et al., 2015; Yue et al., 2017). The exocyst was first shown by negative stain EM to be a stable octameric complex formed by two subcomplexes that interact to form a holo-complex composed of tightly packed helical rods (Heider et al., 2016). Recent cryo-EM and cross-linking studies shed light on the subunit locations within the octameric complex and identified two CorEx motifs that tightly unite four subunits within each subcomplex (Mei et al., 2018). Importantly, this study opened the way for detecting changes in the exocyst structure that facilitate regulation of vesicle tethering as well as downstream SNARE complex formation.

Members of the Rho/Cdc42 GTPase family are essential determinants of polarity and spatial regulators of exocytosis in yeast (Adamo et al., 1999, 2001; Guo et al., 2001) and animal cells (Pathak and Dermardirossian, 2013; Inoue et al., 2003). In yeast, they are proposed to act in exocytosis through physical interactions with the Exo70 and Sec3 subunits of the exocyst complex (Zhang et al., 2001; Wu et al., 2010). The precise mechanism by which Rho GTPases regulate the exocyst complex is not well understood. Several mechanisms have been proposed, including physical recruitment (Finger et al., 1998; Guo et al., 2001), local assembly/disassembly (Boyd et al., 2004), and local activation of the intact complex through an allosteric mechanism (Roumanie et al., 2005; Heider et al., 2016). We used a genetic screen for suppressors of the Cdc42/Rho3 pathway in exocytosis, which resulted in the identification of gain-of-function mutations in the Exo70 subunit of the exocyst complex (Wu et al., 2010). In support of an allosteric regulatory mechanism, these mutants were found to bypass the need for either Rho3 or Cdc42 regulation of exocytosis without detectably affecting the localization or assembly/disassembly state of the exocyst complex (Wu et al., 2010). Together, these data suggested that Rho GTPases might regulate exocytosis by causing a conformational switch in the exocyst complex from a basal to an activated state and that the gain-of-function mutant complexes may mimic the activated state (Wu et al., 2008).

Here, we make use of a novel cell-free vesicle–vesicle tethering assay to biochemically interrogate how exocyst functions in vesicle tethering in vitro (Rossi et al., 2015). This assay makes use of small amounts of Sro7 to "prime" the system to allow us to detect vesicle–vesicle tethering activity with purified exocyst complex. As previously shown with Sro7 (Rossi et al., 2015), the activity of purified exocyst complex in the assay depends on the presence of Sec4 and is independent of the t-SNAREs Sso1/2 and Sec9. We also demonstrate that in contrast to Sro7-mediated vesicle tethering, the presence of the v-SNARE, Snc1/2, on the surface of the vesicles is crucial for exocyst-mediated tethering to occur in vitro. Importantly, exocyst complexes containing dominant gain-of-function alleles of Exo70 show substantial increases in tethering activity. Structural comparison of gain-of-function exocyst complexes to wild-type complexes reveals critical changes in the conformation of Exo70 that appears to open up a SNARE-binding site within the complex. The structural change is associated with an increased affinity of the exocyst for the v-SNARE Snc2 and is likely responsible for both the increased tethering activity observed in vitro and the genetic suppression of the mutants in the Rho/Cdc42 pathway observed in vivo. Together, these results suggest an allosteric regulatory mechanism used by Rho family GTPases to regulate tethering and fusion at sites of polarized growth with spatial specificity.

Results

Purified exocyst complex stimulates vesicle–vesicle tethering in a reconstituted system

The direct tethering of vesicles by exocyst has not previously been demonstrated in vitro. We recently established an in vitro tethering assay to examine Sro7 function as a downstream effector of the Sec4 Rab GTPase in vesicle tethering (Rossi et al., 2015, 2018). This assay makes use of post-Golgi vesicles isolated from yeast secretory mutant strains, full-length Sro7 protein purified from yeast, and buffer containing $MgCl_2$ and GTPγS. Vesicles labeled with either GFP-Sec4 and/or the lipid dye FM4-64 tether together in the presence of Sro7 to form vesicle clusters visible by fluorescence microscopy or negative stain EM. As the exocyst is also a downstream effector of Sec4 function (Guo et al., 1999a), we asked whether purified exocyst complex would demonstrate a similar activity in this assay (Fig. 1 A). We purified exocyst complexes by fusing a C-terminal tobacco etch virus (TEV)–Myc tag on the Sec8 subunit and subjecting lysates to affinity purification/TEV release, using a protocol similar to our purification of Sro7 (Rossi et al., 2015). SDS-PAGE followed by Coomassie staining and Western blot analyses confirmed that the exocyst complex was present in biochemically tractable quantities and contained all eight subunits, although slight proteolysis of the Sec3 subunit was observed (Fig. 1 C). When exocyst was added in the vesicle–vesicle tethering assay, at ∼10 nM, the purified complex had no detectable effect on vesicle clustering (Fig. 1 A). Since the exocyst and Sro7 pathways show strong genetic and physical interactions in post-Golgi trafficking, we next asked if stimulation of clustering by the exocyst might be detectable when submaximal amounts of Sro7 (∼200 nM) were present in the assay. When purified wild-type exocyst was added to an assay mix under these conditions, we observed a significant dose-dependent increase in vesicle–vesicle tethering compared with the addition of Sro7 alone. This assay (Fig. 1 A) made use of a vesicle-enriched fraction prepared by differential centrifugation of a lysate obtained from a post-Golgi vesicle accumulating yeast strain, *sec6-4* (Rossi et al., 2015). To

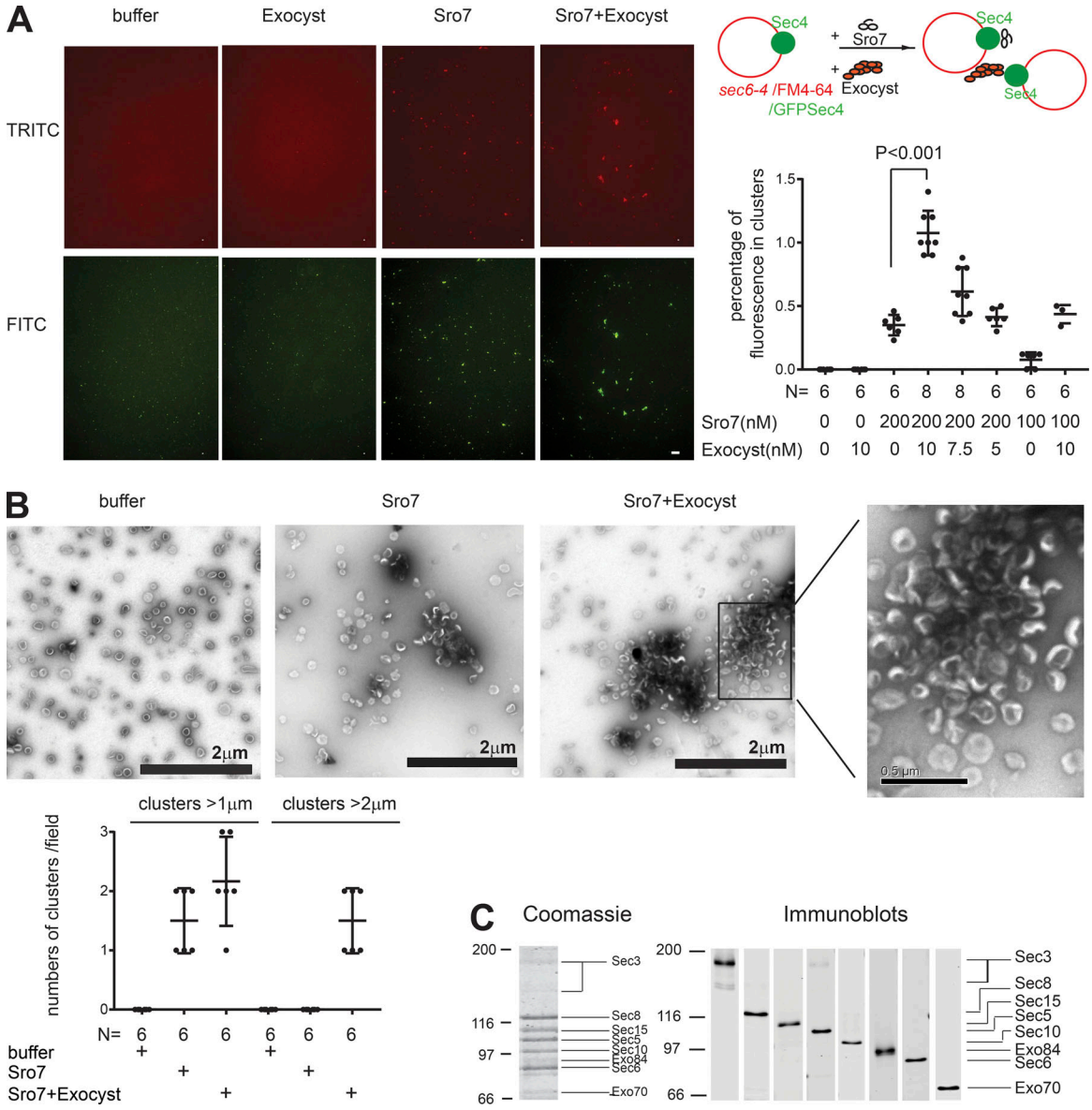

Figure 1. **The exocyst complex and Sro7 function together in an in vitro vesicle–vesicle tethering assay. (A)** Vesicles labeled with the lipid dye FM4-64 were isolated from a *sec6-4* mutant strain expressing GFP-Sec4 and used in an in vitro vesicle–vesicle tethering assay with suboptimal concentrations of purified Sro7 (0.2 μM) and increasing amounts of purified wild-type exocyst complex. Scale bar, 5 μm. Vesicle–vesicle tethering was measured as the percentage of fluorescence seen in clusters over the total fluorescence of the image. Error bar represents SD obtained from counting images at 60× magnification. P values were obtained using a two-tailed Student's *t* test. Data distribution was assumed to be normal, but this was not explicitly tested. **(B)** Vesicles obtained from a *sec6-4* mutant strain were purified on a 20–40% sorbitol velocity gradient and used in an in vitro tethering assay as shown in A. Samples were subjected to negative stain EM, and quantitation was expressed as the number of clusters of different size groups in images taken from six different fields. Error bars represent SD. **(C)** Coomassie stain and immunoblot of purified wild-type exocyst complex used in the tethering assay. A single immunoblot was cut into strips, and each strip was probed with subunit-specific rabbit antisera.

determine whether size-purified post-Golgi vesicles were active in Sro7/exocyst-mediated vesicle–vesicle tethering in vitro, we isolated FM4-64–labeled vesicles from a *sec6-4* mutant strain by sedimentation on a 20–40% sorbitol velocity gradient. Vesicles were then incubated with both Sro7 and the exocyst complex and analyzed by both fluorescence microscopy (not depicted) and negative stain EM (Fig. 1 B). The addition of both the Sec4 effectors resulted in a dramatic increase of clusters containing 80–100 nm post-Golgi vesicles compared with the addition of Sro7 alone.

EXO70 dominant mutants confer an exocytic gain-of-function in vivo and an increase in exocyst vesicle tethering activity in vitro

We previously demonstrated that the Exo70 and Sec3 subunits of the exocyst complex represent critical targets for Rho/Cdc42 regulation of exocytosis (Roumanie et al., 2005; Wu and Brennwald, 2010; Wu et al., 2010). Mutants in *RHO3* (*rho3-V51*) and *CDC42* (*cdc42-6*) demonstrated allele-specific defects in exocytic function without affecting exocyst or Rho/Cdc42 localization. These data suggested that the exocyst is acting as a

vesicle tethering/fusion machine that is positively regulated when engaged by Rho GTPases (Wu et al., 2008). We developed a genetic screen to identify dominant gain-of-function mutant forms of the Rho3/Cdc42 effector subunit Exo70, which might mimic the effect of Rho activation of the complex. The screen succeeded in the isolation of a number of single-residue missense mutations in *EXO70*, which strongly suppressed the growth and secretion defects associated with both *rho3Δ* and *cdc42-6* mutants, even in the presence of wild-type *EXO70* (Wu et al., 2010). The isolation of such mutants is consistent with a model for Rho/Cdc42 regulation of exocyst function that is similar to that observed in other Rho effectors such as formins and PAK (p21 activated kinase) kinases, where binding of the Rho GTPases activates by relief of autoinhibition within the Rho effectors themselves (Otomo et al., 2005, Harms et. al., 2018). Therefore, the dominant suppressing forms of *EXO70* may mimic Rho GTPase activation by promoting the "activated" (or no longer autoinhibited) form of the exocyst, which should increase exocyst tethering activity.

Recently, Masgrau et al. (2017) and Kustermann et al. (2017) identified an important function for the polarity proteins Boi1 and Boi2 in post-Golgi trafficking to the cell surface. In particular, Masgrau et al. (2017) identified a mutant form of *EXO70* as a spontaneous suppressor of a *boi1Δ, boi2Δ* double mutant strain. Interestingly, the sole extragenic suppressor mutant that was identified in this study was *EXO70-G388R*, which was found to act in a dominant fashion and was identical to a dominant suppressor previously isolated in our *rho3Δ/cdc42-6* screen (Wu et al., 2008). To determine if other dominant *EXO70* alleles isolated in our screen also show *boi1/2* suppression, we transformed two strong (G388R and I114F) and one weaker (D541Y) mutant of *EXO70* into the temperature-sensitive *boi1-11, boi2Δ* strain and compared the results to the same mutants transformed into the original *cdc42-6* and *rho3Δ* strains (Fig. 2 A). The two *EXO70* alleles (I114F and G388R), which strongly suppress *cdc42-6* and *rho3Δ*, also demonstrated robust suppression of *boi1-11, boi2Δ*, while the weaker allele, *EXO70-D541Y*, which barely suppressed *cdc42-6*, also showed weaker suppression of the temperature-sensitive growth associated with the *boi1-11, boi2Δ* strain. Clearly the functions of Rho3/Cdc42 and Boi1/Boi2 in exocytosis are closely related, as defects in both pathways are overcome to similar degrees by a common set of gain-of-function mutations within Exo70.

We next biochemically characterized the exocyst complexes containing the mutant Exo70 proteins to examine the mechanism responsible for their genetic gain of function. Previous analyses demonstrated that exocyst complexes containing the gain-of-function Exo70 mutant proteins were identical to wild-type complexes in their subunit composition and stoichiometry (Wu et al., 2010). Therefore, the Rho GTPase activation does not appear to involve assembly or disassembly of one or more subunits of exocyst, but rather suggests an allosteric change in the packing of one or more of the subunits within the complex (Wu et al., 2010). To determine if the tethering activity of the mutant exocyst complexes was affected by the gain-of-function Exo70 subunits, we examined wild-type and mutant exocyst complexes in our in vitro vesicle–vesicle tethering assay. We constructed strains containing wild-type and mutant *EXO70* alleles, as the sole source of Exo70, in yeast cells engineered with a C-terminal TEV/myc-tagged form of Sec8, similar to that used previously except for the addition of the TEV site (TerBush et al., 1996; Wu et al., 2010; see Materials and methods). We purified exocyst complexes from strains containing *EXO70-I144F*, *EXO70-G388R*, *EXO70-D541Y*, or wild-type *EXO70*, making sure to carefully normalize the concentrations of the resulting complexes, using quantitative Western blot analysis of all eight subunits (Fig. 2 C). As with our previous analysis of these Exo70 complexes (Wu et al., 2010), we observed no difference in the subunit composition of these purified complexes (Fig. 2 C). We then tested the tethering activities of these complexes under the conditions described in Fig. 1. The results demonstrated a dramatic increase in tethering when the Exo70-I114F or Exo70-G388R subunit was present in the complex (Fig. 2, B and C). The *EXO70-D451Y* allele, however, demonstrated only a minor increase in tethering activity. None of the three gain-of-function complexes bypassed the requirement for Sro7 in the assay, just as we found that none of the *EXO70* alleles bypassed the requirement for Sro7/77 in vivo (not depicted). These results demonstrate the sensitivity of our tethering assay to the functional state of the exocyst and provide the first biochemical evidence that exocyst tethering activity is up-regulated by gain-of-function mutations in Exo70. Importantly, as these mutants were selected specifically to bypass the need for Rho/Cdc42 activation, we hypothesize that they may mimic the Rho-activated state of the complex (Wu et al., 2010). Additionally, the fact that the dominant Exo70 mutations are separated by considerable distances within the Exo70 ternary structure supports the idea that these mutations bring about an allosteric change to the complex rather than affecting a specific binding site (see Fig. 6).

Negative stain EM demonstrates conformational changes in exocyst structure associated with the activated state of the complex

To identify structural changes to the exocyst that might be associated with the *EXO70* mutants, we purified activated Exo70-G388R and Exo70-I114F mutant complexes for analysis by negative stain EM, as previously described (Heider et al., 2016). The raw micrographs (Fig. S1) revealed particles with size and shape roughly similar to the wild-type exocyst. The use of iterative rounds of unsupervised 2D classification and class averaging resulted in several views of the complexes containing the mutant Exo70 subunits. Comparison of class averages from the wild-type exocyst negative stain data to the mutant's suggested that one or more of the subunits changed conformation. We observed similar changes with both the Exo70-G388R and Exo70-I114F mutant complexes (Fig. S2). To examine these changes in more detail, we compared 3D reconstructions of the wild-type (containing a C-terminal GFP tag on Sec15) and Exo70-I114F exocyst complexes to the recently described cryo-EM structure of the exocyst complex low-pass filtered to 20-Å resolution (Fig. 3).

The most distinct changes in the Exo70-I114F complexes occurred in the regions of exocyst containing Exo70 and Sec6.

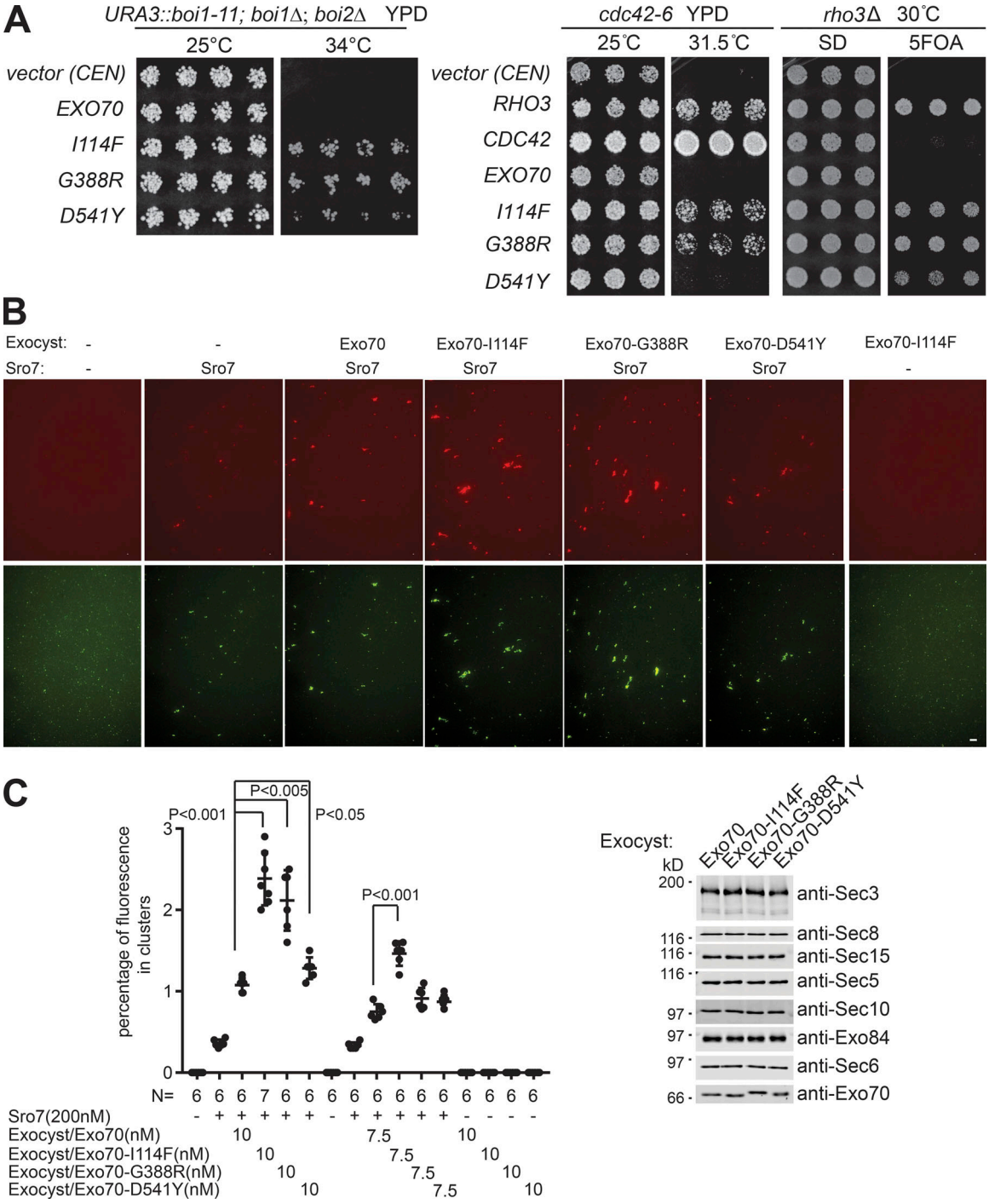

Figure 2. **Gain-of-function alleles of Exo70 that mimic Rho regulation of the exocyst complex up-regulate exocyst function in vesicle–vesicle tethering. (A)** Wild-type *EXO70* and the dominant gain-of-function mutants *EXO70-I114F*, *EXO70-G388R*, *EXO70-D541Y*, and vector only (*CEN*) were transformed into a *RHO3* plasmid shuffle strain, a *cdc42-6* strain, and a *URA3::boi1-11*, *boi1Δ*, *boi2Δ* deletion strain. The growth of three independent transformants is shown for each *EXO70* mutant in the mutant strains analyzed, under permissive and restrictive conditions. **(B)** Vesicles labeled with the lipid dye FM4-64 were isolated from a *sec6-4* mutant strain expressing GFP-Sec4 and used in an in vitro vesicle–vesicle tethering assay with suboptimal concentrations of purified Sro7 (0.2 µM) and identical amounts of exocyst complexes containing wild-type Exo70, Exo70-I114F, Exo70-G388R, or Exo70-D541Y gain-of-function alleles in Exo70. Scale bar, 5 µm. **(C)** Vesicle–vesicle tethering was measured as the percentage of fluorescence seen in clusters over the total florescence of the image. Error bar represents SD obtained from counting images at 60× magnification. P values were obtained using a two-tailed Student's *t* test. Data distribution was assumed to be normal, but this was not explicitly tested. Western blot analysis of exocyst complexes used in B is shown to the right of the quantitation.

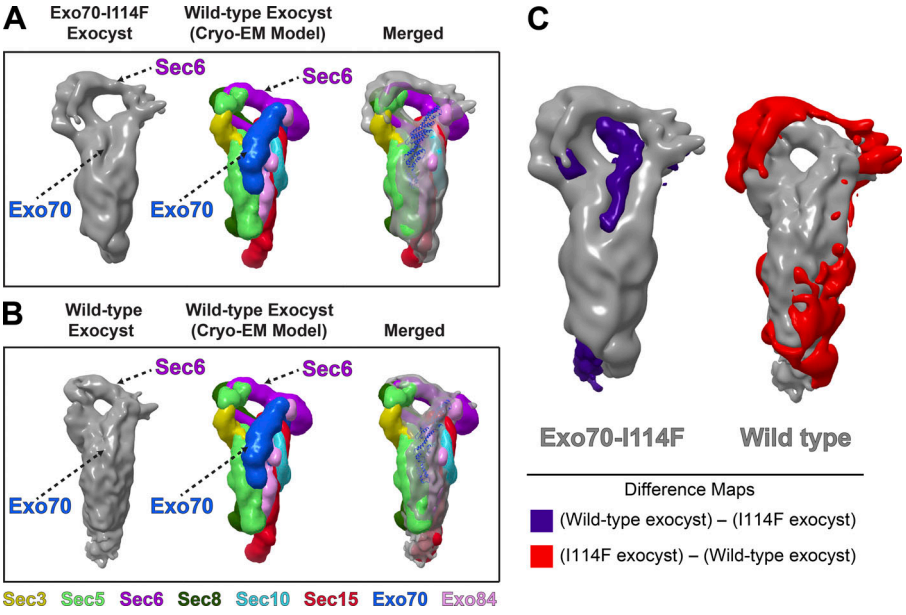

Figure 3. **Exo70-I114F alters the 3D structure of exocyst. (A and B)** Negative stain EM 3D reconstructions of wild-type (Sec15-GFP tagged) and Exo70-I114F exocyst compared with a low-pass filtered representation of the wild-type exocyst determined by cryo-EM (A: Exo70-I114F, B: Sec15-GFP, compared with PDB accession no. 5YFP). Exo70 is well accounted for in the Sec15-GFP reconstruction, but density for Exo70 is largely missing from the Exo70-I114F reconstruction. **(C)** Difference map comparisons of Exo70-I114F and Sec15-GFP reconstructions, highlighting the regions in the difference maps with isosurface values exceeding three SDs. Regions associated with Sec6 and Exo70 are most significantly highlighted in the difference maps (as well as the GFP-tag on the C-terminus of Sec15 in the wild-type structure, but not in the mutant).

Difference maps between the wild-type and mutant 3D negative stain structures revealed significant density difference (greater than three SDs) that can be attributed to changes in both Exo70 and Sec6 (Fig. 3 C). By comparison with the wild-type complex in both negative stain and cryo conditions, the mutant exocyst showed a loss of density at the position expected for Exo70. Several possible explanations exist, including (a) the mutant Exo70 subunit is too flexibly bound to resolve in 2D class averages or 3D reconstructions or (b) the Exo70 subunit dissociated from the complex during negative stain EM preparation. As our biochemical experiments indicated that the exocyst complexes used for the negative stain EM were fully intact, the most probable explanation for this difference is that the mutant Exo70 subunit remained associated with the complex but with substantially increased dynamics, precluding coherent alignment and averaging.

To exclude the possibility that the mutant Exo70 had dissociated, we used 5-nm Ni-NTA gold particles to label C-terminally His_6-tagged wild-type Exo70 and Exo70-I114F exocyst complexes in negative stain EM. We found that the gold particles labeled both wild-type and mutant complexes with a similar labeling efficiency, suggesting that the Exo70 mutant subunits remain associated with the exocyst complex on the negative stain grids (Fig. S3). Therefore, we conclude that the mutant Exo70 subunits are highly mobile/dynamic compared with the other exocyst subunits, but remain bound to the exocyst complex, presumably through interactions of its N-terminal CorEx motif.

The consequences of increased Exo70 mobility within this structure are especially apparent at the wider end of the complex, where the cryo-EM structural model shows that the Sec6 subunit crosses over the top to form a "cap" (Fig. 3). In this region of the structure, there is a pronounced "hole" or absence of density in the activated complexes compared with wild-type exocyst (projection and negative stain; Figs. 3 and S2). None of the other exocyst subunits appear to be markedly shifted in the mutant complexes, except that Sec6 appears less well resolved, again consistent with increased dynamics. Opening of a hole next to the Sec6 cap and increased Sec6 dynamics may critically affect several known binding interactions between exocyst and components of the exocytic fusion machinery. In particular, this region contains the binding site for the v-SNARE Snc1/2, which is important for the stable association of exocyst with post-Golgi vesicles (Shen et al., 2013). This region also contains binding sites for the plasma membrane SNARE Sec9, ternary SNARE complexes (Dubuke et al., 2015), and the SNARE regulator Sec1 (Morgera et al., 2012).

Exocyst complexes containing gain-of-function Exo70 show a significant increase in affinity for the v-SNARE Snc2

To determine if the affinity of the interaction of the exocyst with the v-SNARE Snc2 is measurably altered in exocyst complexes containing the gain-of-function alleles of Exo70, we performed binding experiments using purified exocyst and GST beads containing the cytoplasmic domain of Snc2. As a control, we used a Snc2 protein containing two point mutations that were previously shown to block the interaction with Sec6 (Snc2-R79E and K82E; Shen et al., 2013). Purified wild-type exocyst complexes bind readily to GST-Snc2 but do not bind to the GST-Snc2 (R79E, K82E) control beads (Fig. 4 A). When either of the two gain-of-function exocyst complexes (Exo70-I114F or Exo70-G388R) was examined, we observed a significant and reproducible increase in binding to GST-Snc2, but no binding to control beads (Fig. 4 A). To further characterize the change in affinity for Snc2 associated with activation of the exocyst, we performed saturation binding analysis on wild-type and Exo70-I114F exocyst complexes using a range of GST-Snc2 protein concentrations. We monitored binding by immunoblot analysis with antisera against either Exo84 or Exo70 subunits of the exocyst. The results of two such experiments were averaged and used to generate binding isotherms from which we estimated the apparent K_d for each complex with GST-Snc2 (Fig. 4 B). The results demonstrate a very pronounced increase in affinity (or

reduction in apparent K_d) in response to the activating Exo70-I114F mutation. Therefore, the structural changes that cause increased accessibility at the Sec6 cap correlate with a significant increase in binding affinity between the activated exocyst and Snc2 in this assay. These results are consistent with the notion that the genetic and biochemical gain-of-function properties of these mutants are, at least in part, a result of the increased affinity of the activated exocyst for the v-SNARE Snc.

Exocyst tethering activity requires both the Rab GTPase Sec4 and the v-SNARE Snc1/2 on the vesicle surface

Shen et al. (2013) have proposed that the exocyst is recruited to secretory vesicles by the combined signals of Sec4-GTP and Snc1/2. We, therefore, wanted to examine if the interactions with Sec4 and Snc1/2 were necessary for the biochemical activity of the wild-type and activated exocyst complexes in the in vitro tethering assay. To examine the requirements for Sec4, or any of the three exocytic SNARE proteins, Snc1/2, Sso1/2, and Sec9, we generated FM4-64–labeled vesicles from secretory mutant strains of Sec4 (*sec4-8*), Snc1/2 (*snc1Δ*; *snc2Δ + GAL-SNC1*), Sso1/2 (*sso1-1*; *sso2Δ*), and Sec9 (*sec9-4*) and normalized the concentration of vesicles using Western blot analyses of vesicle marker proteins (Sec4, Ypt31/32, Snc1/2, and Sso1/2). We then tested these vesicles in our in vitro vesicle–vesicle tethering assay with Sro7 alone or exocyst plus Sro7. As previously shown, Sro7-mediated vesicle tethering was dependent on functional Sec4 on the surface of secretory vesicles (Rossi et al., 2015; Fig. 5, A and B). This result was similar when Sro7 and exocyst were both added (Fig. 5, A and B). However, unlike results obtained with Sro7 alone (Rossi et al., 2015; Fig. 5 A), the exocyst increased vesicle tethering only if a functional v-SNARE Snc1/2 was present on the surface of vesicles. In other words, there was no increase in vesicle tethering when vesicles lacked the v-SNARE Snc1/2 (Fig. 5, A and B). These data suggested that while Sro7 does not require SNARE proteins to mediate vesicle tethering, the exocyst complex requires a functional v-SNARE for vesicle tethering to occur (Fig. 5 B). As an additional confirmation of the requirement for Snc2 during Sro7/exocyst-mediated tethering, we analyzed the effect of soluble Snc2 (lacking the transmembrane domain) on the ability of exocyst to stimulate vesicle–vesicle tethering in vitro. The presence of excess soluble Snc2 added to the assay would be expected to compete with endogenous Snc1/2 present on the vesicle surface. We found that wild-type but not the mutant (R79E, K82E) Snc2 protein (a mutant that cannot bind the exocyst) inhibits vesicle–vesicle tethering in a concentration-dependent manner (Fig. 5 D). Taken together, these data are in full agreement with the suggestion that recognition of Snc1/2 and Sec4 by the exocyst allows coincidence detection of the vesicle surface, providing an additional level of specificity to post-Golgi vesicle tethering (Shen at al., 2013).

Discussion

Here we describe the first biochemical assay demonstrating a role for the exocyst complex in post-Golgi vesicle tethering. We accomplished this by modifying an assay we previously developed to examine the role of another post-Golgi tethering protein, the yeast tomosyn homologue, Sro7. Both Sro7 and the exocyst complex are thought to act as direct effector proteins for the post-Golgi vesicle Rab GTPase, Sec4 (Grosshans et al., 2006; Guo et al., 1999a; Watson et al., 2015). Consistent with a role for both these effector proteins as vesicle tethers, we show that both Sro7 and the exocyst require functional Sec4 on the vesicle surface for tethering to occur in vitro. However, unlike Sro7, the exocyst also requires the v-SNARE Snc1/2 on the vesicle surface for vesicle tethering to occur. It is presently unclear, however, if this requirement occurs on the same or opposing membranes. Importantly, we find that the intact eight-subunit exocyst complex is capable of tethering post-Golgi vesicles to each other and that equivalent amounts of exocyst complexes containing gain-of-function Exo70 mutants show dramatic increases in tethering activity in vitro. The function of the exocyst in vivo is thought to be in Rab-dependent tethering of Golgi-derived vesicles with the cell surface (Munson and Novick, 2006; Nejsum and Nelson, 2009). Therefore, the pronounced correlation between the genetic effect of these mutants in vivo and the biochemical effect in vitro strongly suggest that this novel assay reflects this central property of the exocyst complex. The tethering assay described here involves homotypic tethering of post-Golgi vesicles, yet many of the features present in exocyst-mediated vesicle tethering in this in vitro assay closely resemble vesicle tethering events that are thought to occur before fusion with the target membrane. The most important similarity is the requirement in both cases for GTP-bound Rab protein and direct Rab effectors in the formation of close physical apposition of a vesicle with an opposing membrane. Also, the requirement for the interaction of the v-SNARE Snc with the exocyst, which is critical for tethering in the assay, has also been shown to be important for normal (heterotypic) exocytic transport in vivo (Shen et al., 2013). We anticipate that further development of this assay will allow us to directly detect the role of the exocyst in heterotypic vesicle tethering of post-Golgi vesicles with "plasma membrane–like" membranes.

To understand the change in the exocyst complex activity observed in vivo and in vitro, we used negative stain EM with 2D particle averaging and 3D particle reconstruction to characterize any distinct structural differences between the gain-of-function and wild-type complexes. Our previous 2D negative stain images and 3D model of wild-type exocyst are remarkably consistent with a 3D cryo-EM structural model (Mei et al., 2018; Fig. 3). Therefore, we compared our negative stain 3D model of the Exo70-I114F complex with both the wild-type negative stain model and the cryo-EM–derived structure, to identify changes that occurred as a consequence of the mutant Exo70 subunit (Fig. 3). We observed that for complexes containing the I114F mutation, the Exo70 mutant subunit showed increased dynamics, leading to a "hole" nearby the Sec6 protein, as well as additional flexibility of Sec6. Interestingly, although the 2D images for the Exo70-G388R mutant complex are almost indistinguishable from that of the Exo70-I114F mutant complex, these gain-of-function mutations in Exo70 are not located near each other in the wild-type structure (Fig. 6). Isoleucine 114 is located in the first helical bundle (termed A; Dong et al., 2005), very

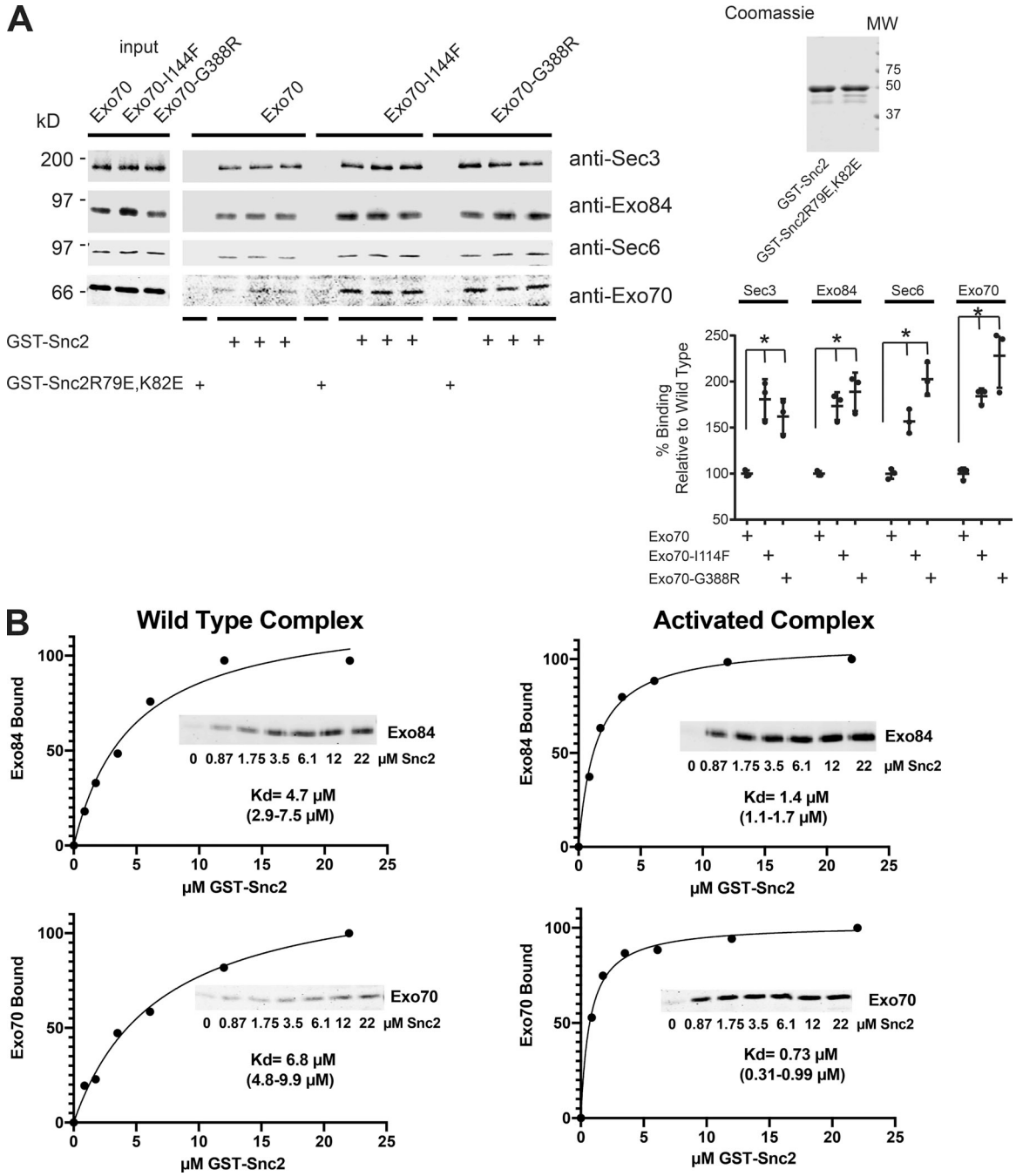

Figure 4. **The gain-of-function alleles of Exo70 increase exocyst complex binding to the v-SNARE Snc2. (A)** Purified wild-type exocyst complexes and exocyst complexes containing Exo70-I114F or Exo70-G388R were used in a GST pulldown assay with GST-Snc2 or GST-Snc2R79E, K82E immobilized on beads. Quantitation of the binding and Coomassie stain of GST-fusion proteins are shown to the right. Error bars represent SD. P values were obtained using a two-tailed Student's *t* test. *, $P < 0.05$. Data distribution was assumed to be normal, but this was not explicitly tested. **(B)** Saturation binding analysis of wild-type exocyst or activated exocyst complexes containing Exo70-I114F. Complexes were examined in binding assays with varying amounts of GST-Snc2 immobilized on beads. Binding results are the average of two biological replicas, and the amount bound was normalized to the highest amount bound for each experiment. Shown is a representative immunoblot for each binding experiment. The apparent K_d for each subunit was determined using GraphPad Prism with 95% confidence limits shown below.

close to where the bundle connects with the CorEx helices, and where Exo70 makes a sharp bend to pack alongside other exocyst subunits. The I114F mutation could affect the stability of bundle A, or perhaps the packing of Exo70 against Exo84 or Sec6. Glycine 388, however, is located further down the bundles at a hinge between the B–C bundles. The G388R mutation likely destabilizes bundle C, as it does not appear to be in a region of Exo70 that interacts with other exocyst subunits. The mutation from G to R could lead to steric clashes that weaken the region between B and C, making this region more flexible and perhaps

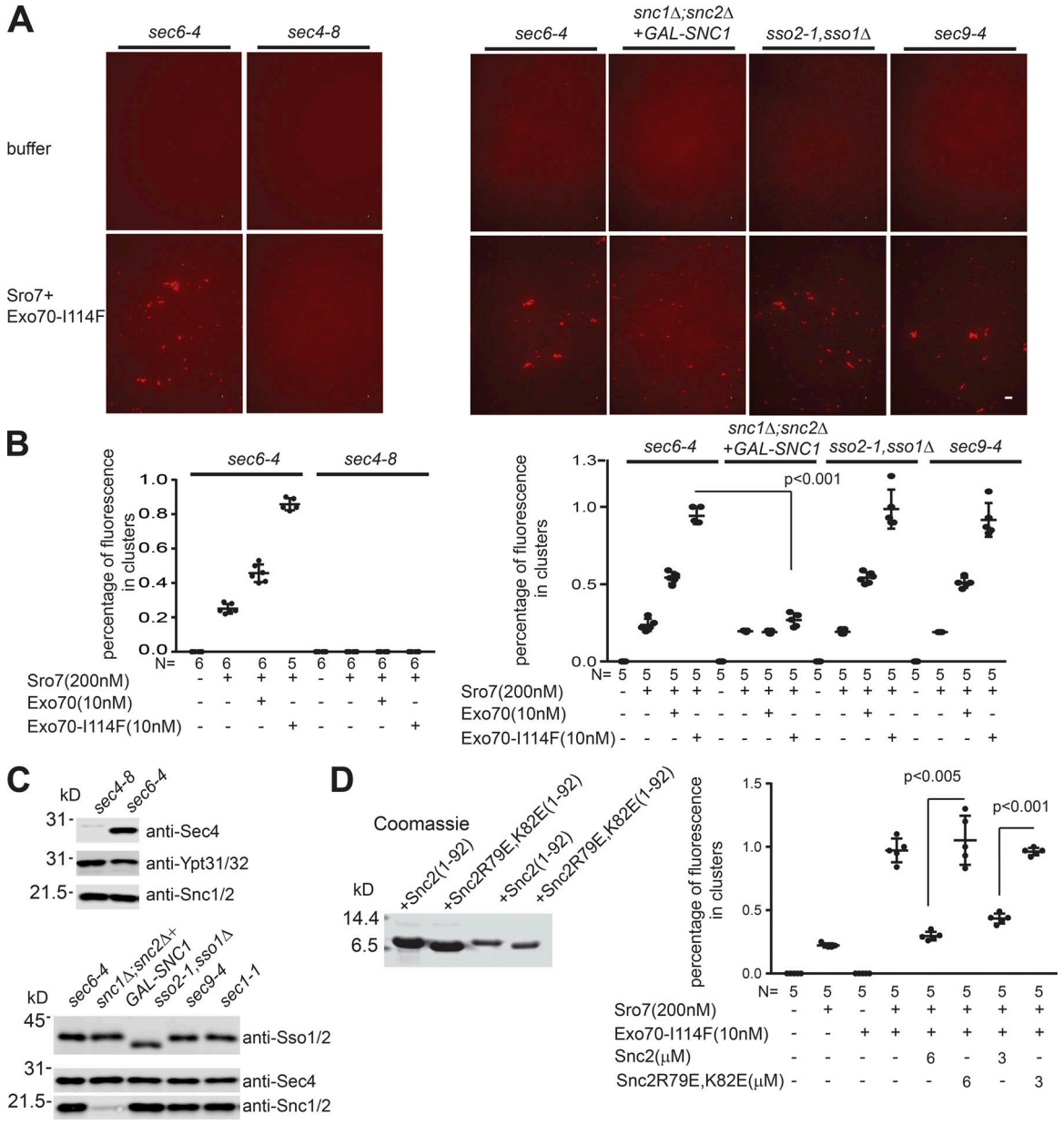

Figure 5. **The exocyst complex requires functional Sec4 and Snc2 on the vesicle surface to mediate in vitro vesicle tethering in the presence of Sro7.** **(A)** Vesicles generated from the yeast secretory mutant strains defective in the exocyst subunit Sec6 (*sec6-4*), the Rab GTPase Sec4 (*sec4-8*), or the SNARE proteins Sec9 (*sec9-4*), Sso1/2 (*sso1Δ;sso2-1*), and Snc1/2 (*snc1Δ;snc2Δ +GAL*-Snc1) were used in an in vitro tethering assay with Sro7 and wild-type exocyst complex or gain-of-function alleles in Exo70 (Exo70-F114). Scale bar, 5 µm. **(B)** Quantitation of the tethering assay is expressed as percentage of fluorescence in the clusters over the florescence of the whole image. Images were taken at 60× magnification. P values were obtained using a two-tailed Student's *t* test. Data distribution was assumed to be normal, but this was not explicitly tested. **(C)** Western blot analysis of normalized vesicle fractions used in A. **(D)** Coomassie staining of wild-type cytoplasmic (1–92 amino acids) Snc2 and mutant Snc2-R79E, K82E used in a vesicle tethering assay with Sro7 and exocyst complex (Exo70-I114F). Quantitation is expressed as the percentage of fluorescence in clusters over the total fluorescence of the image as shown for B.

causing a more global destabilization of Exo70 packing against multiple exocyst subunits. Furthermore, D451Y, which has a weak phenotype in the vesicle–vesicle tethering assay, is at the end of the D bundle; D451Y could destabilize bundle D, which loosely packs against Sec5.

Why do the G388R and I114F mutants have a similar strong phenotype in our assays? The cryo-EM model and previous binding studies (Dong et al., 2005; Heider et al., 2016; Croteau et al., 2009) suggest that the Exo70 C-terminal A–D bundle region is rather loosely bound to the other subunits, through a metastable collection of weak protein–protein interactions. Disruption of one of these interactions may be sufficient to release A–D from its conformation. The region of Sec6 identified as important for binding Snc2 (~292–411; Shen et al., 2013) is located near the region where the Exo70 A bundle packs against Sec6; this packing may occlude the Snc1/2 binding site while the exocyst is in a basal state. The release of this bundle by destabilizing the A–D packing should allow Snc1/2 access to bind Sec6.

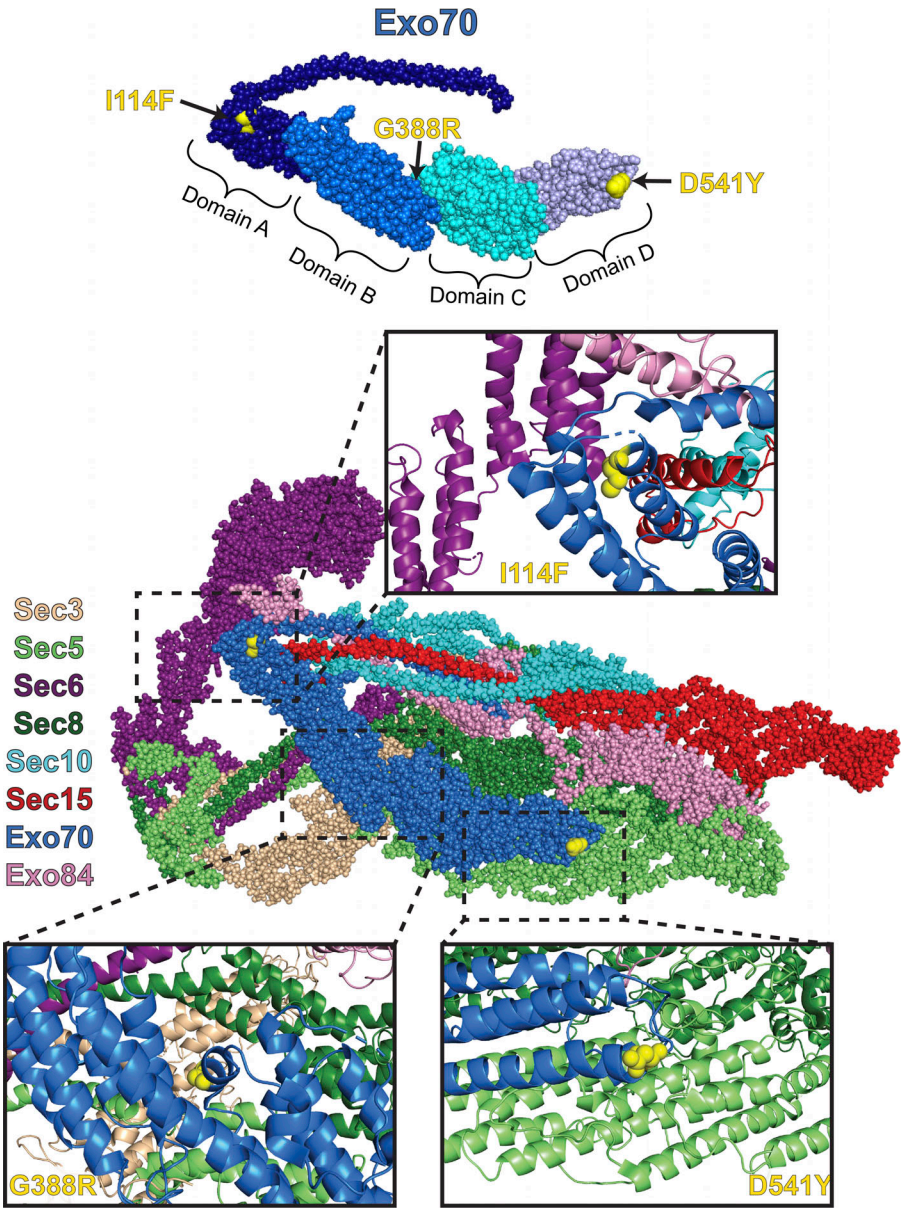

Figure 6. **Sites of Exo70 mutants within the cryo-EM model for the exocyst complex.** Cryo-EM model of the exocyst complex (Mei et al., 2018; PDB accession no. 5YFP), with Exo70 shown in blue and the gain-of-function mutants indicated as yellow spheres. Top: The Exo70 subunit is shown in isolation, with domains A–D specifically labeled in relation to the position of the I114F, G388R, and D541Y point mutations. Insets show zoomed-in views of the close apposition of the Exo70 mutant residues with Sec6 (purple), Exo84 (pink), Sec15 (red), Sec8 (dark green), and Sec5 (light green). Negative stain data indicates increased flexibility throughout the entire A–D region of Exo70, with concomitant effects on Sec6.

Binding studies with the gain-of-function complexes strongly support this idea, as we observed significant increases in binding to Snc2 in response to these mutations.

How does the increased "openness" of Sec6 to binding of the v-SNARE Snc2 contribute to increased tethering activity? Shen et al. (2013) identified a critical role for the v-SNAREs Snc1/2 in recruiting exocyst complexes to vesicles in vivo. This interaction, along with the interaction of the exocyst with Sec4, was proposed to be part of a "coincidence detector" function of the exocyst that would ensure specificity in the types of vesicles that it would be capable of tethering. Indeed, in our in vitro tethering assay, both Sec4 and Snc1/2 are required for exocyst-mediated tethering. This leads us to a simple model by which the gain-of-function mutants act to increase tethering by increasing the availability of exocyst to interact with the v-SNARE on the vesicle surface. Therefore, the more effective the recruitment of exocyst complexes to the vesicle surface, the more efficient the overall tethering of the vesicles both in vitro to each other as well as in vivo to the plasma membrane.

What do the gain-of-function Exo70 results tell us about the role of Rho/Cdc42 GTPases as spatial regulators of exocytosis? The gain-of-function mutants examined here were identified in a genetic screen for *EXO70* alleles that could bypass the requirement for Rho3 and Cdc42 function in exocytosis. We propose a mechanism by which Rho3/Cdc42 activates the exocyst complex by inducing a conformational switch from a basal to an activated state. In support of this, we found that the gain-of-function mutants in Exo70 do not affect the localization or the assembly/disassembly state of the exocyst complex in vivo (Wu et al., 2010). Analysis of the activated complexes in the in vitro tethering assay demonstrated that the gain-of-function activity observed in vivo correlated with an increase in vesicle tethering activity in vitro. This suggests that Rho3/Cdc42 engagement of the exocyst shifts the complex to an activated state, which would

increase exocytic activity by increasing vesicle tethering at sites marked by high concentrations of Rho3/Cdc42. Moreover, while the in vitro vesicle tethering assay is able to recapitulate the gain-of-function phenotype of the Exo70 dominant mutants, the in vivo gain-of-function may well extend beyond the biochemical phenotypes observed here. In particular, the conformational changes observed in response to the two strongest *EXO70* alleles (I114F and G388R) may also affect downstream SNARE assembly events at the plasma membrane. The binding site for the t-SNARE Sec9, the SNARE complex, and Sec1 all reside in the Sec6 cap area of the exocyst (Dubuke et al., 2015; Morgera et al., 2012). Therefore, it is possible that the increased accessibility of this critical region of the exocyst associated with the gain-of-function mutants may impact both the tethering and SNARE assembly functions of the exocyst. Importantly, our identification of a specific conformational change in the exocyst associated with the Exo70 mutants is likely to be a key step forward in understanding the mechanism by which Rho/Cdc42 GTPases spatially regulate exocytosis.

Materials and methods

Plasmids/strains

Wild-type *EXO70* and the *EXO70* dominant mutations were introduced as the sole source of Exo70 in the cell by transformation of an *EXO70* plasmid shuffle strain containing a *KAN* deletion of *EXO70*, with *CEN, LEU2* plasmids containing wild-type *EXO70* or the dominant mutations, followed by counter-selection of the wild-type *EXO70-URA3* plasmid on 5-FOA plates.

The *boi1-11* temperature-sensitive allele was a gift from Daniel Lew's group (Duke University, Durham, NC) and was isolated by random mutagenesis of *BOI1*. The version of the allele used in this study (BY2259: *boi1Δ::hph, boi2Δ::kan; URA3::boi1-11; leu2-3,112*) contains the *boi1-11* allele integrated at the *URA3* locus, along with a deletion in *boi1* marked with hygromycin resistance and a deletion in *boi2* marked with kanamycin resistance. Resulting strain: BY3190: Mat a; *exo70Δ::KAN^R; ura3-52; leu2-3,112; his3Δ200+pRS316-EXO70*.

To generate a 3XMYC tag at the C-terminus of chromosomal Sec8, a fragment containing 1.7 kb of C-terminal *SEC8* in frame with a TEV site followed by a 3MYC tag was introduced as a NotI-KpnI fragment in pRS306. The plasmid was then linearized with XbaI to direct chromosomal integration and generate a single functional copy of *SEC8* containing a C-terminal TEV-3XMYC tag in strains containing a wild-type (*EXO70*) or gain-of-function mutant in *EXO70* (*EXO70-I114F*, *EXO70-G388R*, *EXO70-D541Y*) as the only copy of *EXO70* in the cell. Resulting strain BY3216: *exo70Δ::KAN^R; SEC8-TEV3XMYC::URA3; ura3-52; leu2-3,112; +pRS315-EXO70*; strain BY3218: *exo70Δ::KAN^R; SEC8-TEV3XMYC::URA3; ura3-52; leu2-3,112; +pRS315-EXO70-G388R*; strain BY3220: *exo70Δ::KAN^R; SEC8-TEV3XMYC::URA3; ura3-52; leu2-3,112; +pRS315-EXO70-I114F*; and strain BY3221: *exo70Δ::KAN^R; SEC8-TEV3XMYC::URA3; ura3-52; leu2-3,112; +pRS315-EXO70-D541Y*.

To generate a Protein A tag at the C-terminus of chromosomal *SEC15*, a fragment containing C-terminal *SEC15* in frame with a PreScission protease site followed by a ProteinA(PrA) tag was generated by PCR from a plasmid (pProtAHIS5, a gift from M. Rout, Rockefeller University, New York, NY) as described in Heider et al. (2016) and integrated into yeast containing wild-type *EXO70* or gain-of-function alleles in *EXO70* on a *CEN, LEU2* plasmid. Resulting strain: MMY1075: *SEC15-PrA::HIS5; his3Δ1; ura3-52; leu2Δ0, met15Δ0*; and strain MMY1703: *exo70Δ:: KAN^R; SEC15-PrA::HIS5; his3Δ1; ura3-52; leu2Δ, met15Δ0; +pRS315-EXO70-I114F*.

Wild-type *SNC2* without a transmembrane domain was subcloned as a NdeI-BamHI fragment into a pET15b vector and used to generate soluble Snc2 by nickel column purification. This construct was created using nested primers Snc2-PT1 and Snc2-PT3 with downstream oligo Snc2-PT2b (see below) to amplify the Snc2 cytosolic domain without the internal Nde1 site.

Mutant *SNC2-R79E, K82E* without a transmembrane domain was subcloned in an identical manner to the wild-type protein and subjected to the same nickel column purification. Both wild-type and mutant proteins were dialyzed into 20 mM Tris, pH 7.5, 150 mM sodium chloride, and 10% glycerol. Wild-type *SNC2* and mutant *SNC2-R79E, K82E*, both lacking a transmembrane domain, were also subcloned as SalI-BamHI fragments into a pGEX-6P6H vector (N-terminal GST tag and C-terminal 6xHis tag).

Primers

Primers usedwere Snc2-PT1: 5′-GAGTCACGCATATGTCGTCATCAGTGCCATACGATCCA-3′, Snc2-PT2: 5′-GAGTCACGCGGATCCTTAGCTGAAATGGACGACGATAGGAAC-3′, Snc2-PT3: 5′-CATCAGTGCCATACGATCCACATGTGCCTCCAGAGGAGAGTAAC-3′, F-Sec15-ppx-PrA: 5′-GTCATTGACTCTAATACGAGTAGGATAGCCAAATTTTTTAATAGACGTGGCCTGGAAGTTCTGTTCCAGGGGCCCAGCGGTGAAGCTCAAAAACTTAAT-3′, and R-Sec15-ppx-PrA: 5′-CTTTCTTATGAACGTACAAATGATTATACTGAGATAATATCTAATTTTGTCGACGGTATCGATAAGCTT-3′.

Antibodies

Custom antibodies were from the Brennwald or Munson laboratory collections as noted below. Anti-Sec3: rabbit polyclonal (CUMC147, Brennwald laboratory); anti-Sec8: rabbit polyclonal (Munson laboratory); anti-Sec15: rabbit polyclonal (CUMC140, Brennwald laboratory); anti-Sec5: rabbit polyclonal (CUMC148, Brennwald laboratory); anti-Sec10: rabbit polyclonal (Munson laboratory); anti-Exo84: rabbit polyclonal (Munson laboratory); anti-Sec6 rabbit polyclonal (Munson laboratory); anti-Exo70: rabbit polyclonal (CUMC118, Brennwald laboratory); anti-Sec4: mouse monoclonal (mAb1.2.3, Brennwald laboratory); anti-Snc1/2: rabbit polyclonal (CUMC6, Brennwald laboratory); anti-Sso1/2 rabbit polyclonal (CUMC36, Brennwald laboratory); and anti-Ypt31/32: rabbit polyclonal (CU18).

Exocyst purification

Yeast strains containing a chromosomal copy of C-terminally–tagged 3XMYC Sec8 and plasmids (*CEN*) expressing wild-type Exo70 or the dominant mutations of Exo70 were grown overnight to mid-log phase ($OD_{1.5}$) in synthetic medium with 2% glucose at 30°C. Cells were then shifted to yeast extract peptone dextrose (YPD; 2% glucose) for 2 h to a final OD_3, before adding sodium azide and sodium fluoride to 20 mM final. Cells were then spun at 6,700 g_{max} in a JLA10.5 rotor for 6 min and washed into 10 mM Tris, 20 mM sodium azide, and 20 mM sodium

fluoride before freezing on dry ice. Approximately 50 g of cells was lysed in a bead beater in 20 mM Pipes, pH 6.8, 120 mM sodium chloride, 1 mM EDTA, 0.5% IGEPAL CA-630, 1 mM DTT, and protease inhibitors (2 µg/ml leupeptin, 2 µg/ml aprotinin, 2 µg/ml antipain, 14 µg/ml pepstatin A, 2 mM 4-(2-aminoethyl) benzene-sulfonyl fluoride, and HCl). The lysate was then spun at 17,418 g_{max} for 10 min at 4°C in a JA25.5 rotor, and the supernatant was removed and spun again at 50,000 g_{max} for 30 min in a 41Ti rotor. The lysate concentration was adjusted to 30 mg/ml before preclearing with Sepharose beads for 1 h at 4°C to reduce nonspecific binding. The lysate was then spun for 5 min to remove the Sepharose beads and incubated overnight on ice with 1.0 ml of anti-myc (9E10) antibody. PrA Sepharose beads (1 ml) were added for 2 h at 4°C. The PrA Sepharose beads were washed three times in lysis buffer and then two times in cleavage buffer (20 mM Tris, pH 7.4, 140 mM sodium chloride, 0.1 mM EDTA, and 1 mM DTT) before cleavage in 1 ml of cleavage buffer with TEV enzyme for 4 h at 17°C. After removal of the PrA Sepharose beads, the exocyst complex was collected and frozen.

Sro7 purification

Sro7 was purified as described in Rossi et al. (2015). N-terminal Protein A–tagged Sro7 was expressed behind an *ADH1* promoter from a high copy plasmid in a yeast *pep4Δ* background strain. Approximately 5 liters of cells were grown overnight in synthetic medium to an OD_{599} of 3.0 and then shifted to yeast extract peptone (YP) + 2% glucose for one doubling time. Cells were then harvested and washed in 200 ml of ice-cold buffer containing 10 mm Tris, pH 7.8, 20 mm sodium azide, and 20 mm sodium fluoride to yield a final wet weight of ∼50 g of cells. Cells were frozen on dry ice and stored at −80°C. Lysis was obtained with a bead beater using ice-cold buffer containing 20 mm Tris, pH 7.8, 150 mm NaCl, 0.5% Tween 20, 1 mm DTT, and protease inhibitors (2 µg/ml leupeptin, 2 µg/ml aprotinin, 2 µg/ml antipain, 14 µg/ml pepstatin A, and 1 mm phenylmethylsulfonyl fluoride). Five cycles of 1-min bead beating, followed by 2-min intervals on ice, were used to lyse the cells. The lysate (60 ml) was then spun at 17,400 g_{max} for 10 min at 4°C in a JA25.5 rotor before further dilution (120 ml) and ultracentrifugation at 140,000 g_{max} for 30 min at 4°C in a type 45Ti rotor to yield a final protein concentration of ∼25 mg/ml. Binding to Sepharose CL-6B beads (1 ml of beads/45 ml of lysate) for 1 h at 4°C was used to preclear the lysate before binding to 1 ml of IgG-Sepharose beads for 2 h at 4°C. Beads were washed five times with lysis buffer, three times with lysis buffer containing 400 mm NaCl, and three times with ice-cold cleavage buffer containing 20 mm Tris, pH 7.8, 150 mm NaCl, 0.1 mm EDTA, and 1 mm DTT. Beads were resuspended 1:1 in cleavage buffer, and cleavage was obtained with TEV cleavage enzyme for 5 h at 17°C (5,000 units of TEV/3-ml bed volume beads). Supernatant containing the cleaved protein was collected and frozen at −80°C.

Generation of GFP-Sec4– and FM4-64–labeled vesicles for the in vitro assay

Vesicles labeled with GFP-Sec4 and/or FM4-64 were prepared as described in Rossi et al. (2015). Briefly a *sec6-4* secretory mutant strain expressing GFP-Sec4 (*CEN*) was grown overnight in selective medium to an OD_{599} of 0.6 and shifted for 1 h into YP with 2% glucose before placing the cells at the restrictive temperature of 36°C for 2 h. Sodium azide was added to 20 mM final, and 350 absorbance units were centrifuged and washed into 10 ml of ice-cold 10-mM Tris, pH 7.5, and 20 mM sodium azide. Cells were spheroplasted in 10 ml of buffer (0.1 M Tris, pH 7.5, 1.2 M sorbitol, 10 mM sodium azide, 21 mM β-mercaptoethanol, and 0.05 mg/ml Zymolyse 100T) for 30 min at 37°C and lysed in 4 ml of ice-cold buffer (10 mM triethanolamine, pH 7.2, and 0.8 M sorbitol) containing protease inhibitors (2 µg/ml leupeptin, 2 µg/ml aprotinin, 2 µg/ml antipain, 14 µg/ml pepstatin A, and 1 mM phenylmethylsulphonyl fluoride). The lysate was then spun at 4°C to remove unbroken cells, followed by a spin at 30,000 g_{max} for 15 min in a Sorvall centrifuge to preclear large membranes. 2.5 ml of supernatant was labeled on ice for 10 min with the lipid dye FM4-64 (1 µg/ml). The labeled lysate was layered over 2 ml of an ice-cold sorbitol cushion (20% wt/vol sorbitol in 10 mM triethanolamine, pH 7.2) and centrifuged at 128,000 g_{max} for 1 h at 4°C. The final high-speed pellet was resuspended in 300 µl of lysis buffer, before being aliquoted and frozen at −80°C. For vesicles labeled with FM4-64 alone, the following modifications were made. For the *sec6-4* mutant strain, cells were grown overnight in YP with 2% glucose to an OD_{599} of 0.6 and then shifted to the restrictive temperature of 37°C for 2 h. Cells were treated as above, except 300 absorbance units were spheroplasted in 10 ml of spheroplast buffer before lysis in 4 ml of lysis buffer. The final enriched vesicle fraction, labeled with FM4-64, was resuspended in 600 µl of lysis buffer. For the *sec4-8* mutant strain, 600 absorbance units were spheroplasted in 15 ml of buffer before lysis in 4 ml of buffer and final vesicle resuspension in 600 µl of buffer. For the *sec9-4* and *sso1-1* mutant strains, 300 absorbance units were spheroplasted in 10 ml of spheroplast buffer before lysis and vesicle resuspension in 800 µl of lysis buffer. In the case of the *snc1Δ; snc2Δ* strain containing a (*CEN*) plasmid expressing Snc1 from a *GAL* promoter, cells were grown overnight in YP with 2% raffinose/1% galactose before shifting into YPD (with 2% glucose) for 15 h at room temperature. 700 absorbance units were then spheroplasted in 23 ml of spheroplast buffer and lysed in 9.3 ml of lysis buffer. Vesicles were finally resuspended into ∼500 µl of lysis buffer.

Vesicle purification and EM microscopy

To obtain purified post-Golgi vesicles for negative stain, we used a 128,000 g_{max} pellet, obtained from a *sec6-4* strain as described in the previous section (generation of labeled vesicles). This protocol was modified by increasing the starting amount of cells to 700 absorbance units and resuspending the 128,000 g_{max} pellet in a final volume of 600 µl before loading at the top of 11 ml of linear sorbitol gradient prepared with 1.22-ml steps of 40, 37.5, 35, 32.5, 30, 27.5, 25, 22.5, and 20% sorbitol (wt/vol) in 10 mm triethanolamine acetate, pH 7.2. The gradient was centrifuged at 99,000 g_{max} for 80 min at 4°C and then fractionated into 0.72-µl fractions. Fractions 5–7 (pink color) containing the vesicle fractions were then pooled, diluted with 3 ml of lysis buffer, and centrifuged at 128,000 g_{max} for 1 h. The pellet

fraction containing the purified vesicles was resuspended in 200 µl of lysis buffer.

Purified vesicles were kept on ice and used the following day for the vesicle–vesicle tethering assay described below and then immediately processed for analysis by negative stain EM. The carbon film grids were glow-discharged in a Harrick Plasma Cleaner for 1.5 min. A drop of sample (10 µl) was placed onto a grid that was suspended in reverse forceps for 1 min. The sample was then washed off with 5 drops of 1% aqueous uranyl acetate. The stain was allowed to sit on the grid for 1 min. The grid was blotted on the tip of the forceps with filter paper before air drying and was examined by EM. Quantitation of vesicle clusters by negative stain EM was done by manual counting of vesicle clusters that were >1 or 2 µm in diameter. A minimum of six fields were counted for each condition.

Vesicle–vesicle tethering assay

An enriched vesicle fraction or purified vesicles were pre-incubated with $MgCl_2$ (3 mM) and GTPγS (1 mM) for 30 min on ice before the addition of Sro7 (0.2 µM) and exocyst complex (10 nM) or buffer only for 45 min at 27°C. Vesicle–vesicle clustering was quantitated by taking images at 60× magnification and counting the fluorescence associated with clusters >1 µm over the whole fluorescence of the image. Clusters were identified manually as fluorescent puncta >1 µm in diameter. In cases where vesicle preparations contained both FM4-64 and GFP-Sec4 labels, the TRITC (FM4-64) channel was used for quantification. Each data point represents the summation of fluorescence associated with all the clusters (>1 µm) from a single field divided by the total fluorescence signal in the entire field. A minimum of six fields was used for each condition. All images were acquired using Nikon E600 microscope with a Nikon Planar 60× oil-immersion lens (NA 1.4) using a Photometrics CoolSNAP Dyno charge-coupled device camera. Images were visualized and quantitated using Nikon NIS-Elements software (v4.6).

Binding assay

Binding to GST-Snc2 and GST-Snc2R79E,K82E was conducted using 4 µM GST-Snc2 on beads and ∼2 nM exocyst in binding buffer containing 10 mM Hepes KOH, 140 mM KCl, 0.5% Triton X-100, and 2 mM $MgCl_2$ for 1 h at 4°C. Beads were washed four times in binding buffer and boiled in sample buffer for Western blot analysis with anti-Sec3, anti-Exo84, anti-Sec6, and anti-Exo70 antibodies. For saturation binding studies, the same conditions were used, except binding was allowed to proceed for 2 h at 4°C. Binding data were averaged from two biological replicas after normalizing the amount bound to the highest amount bound for each experiment. The apparent K_d for each subunit was determined using a one-site specific binding model in GraphPad Prism.

Exocyst purification and negative stain EM

Yeast strains containing *SEC15-PrA* and *CEN* plasmids expressing wild-type or the dominant mutants of *EXO70* (as the sole copy of *EXO70*) were grown in 2 liters of YPD to mid-log phase ($OD_{1.5}$). Cells were then spun at 3,000 *g* for 5 min, washed with 50 ml of milli-Q water, and spun again for 15 min at 4,000 *g* to remove excess water. The cell pellet was extruded through a syringe into liquid nitrogen to make noodles, which were stored at −80°C (Oeffinger et al., 2007). Noodles were ground as described in Heider et al. (2016) and stored at −80°C. 750 mg of frozen lysate powder was added to a 15-ml conical tube and resuspended in 3 ml of lysis buffer (40 mM Tris, pH 8.0, 200 mM Na_3Citrate, and 1× cOmplete Mini EDTA-free protease inhibitor solution; Roche Life Science). The solution was vortexed until fully re-suspended, and then spun at 14,000 g for 10 min at 4°C. The supernatant was incubated with 25 µl of rabbit IgG-magnetic beads (Hakhverdyan et al., 2015) for 1 h at 4°C, nutating. The beads were washed in lysis buffer, and then the exocyst complex was cleaved in 30 µl of lysis buffer (without cOmplete Mini EDTA-free protease inhibitor solution) with PreScission protease (GE Healthcare) for 1.5 h. Negative stain EM grids were prepared by absorbing 6 µl of the exocyst sample onto glow-discharged carbon-coated 400-mesh copper grids (EMS) and staining with 0.75% uranyl formate.

Gold labeling of Exo70

Yeast strains containing *SEC8-PrA* and *CEN* plasmids expressing *EXO70* or *EXO70-I114F* (as the sole copy of *EXO70*) with a C-terminal His_6-tag were grown and harvested for exocyst purification as described above. After PreScission cleavage, but before application onto the carbon-coated grids, the exocyst sample was incubated with a 1:10 dilution of 5 nm Ni-NTA nanogold particles (nanoprobes) for 10 min. 6 µl of sample was then absorbed onto glow discharged carbon-coated 400-mesh copper grids (EMS) and stained with 0.75% uranyl formate.

Negative stain imaging and data processing for 2D projections in Fig. S2

Exocyst and exocyst mutants were imaged with a Tecnai T20 microscope (FEI) equipped with a LaB6 filament, operated at 200 kV. Micrographs were collected with a TemCam-F816 8 × 8K camera (T-VIPS) using SerialEM software, with a nominal pixel size of 3.14 Å and a defocus range of 0.7–1.7 µm. The parameters of the contrast transfer function (CTF) were estimated using GCTF v1.06; automated particle picking was done using Gautomatch-v0.53; and all alignments and averages were computed using Cryosparc v0.6.5 (Zhang 2016; Punjani et al., 2017).

3D negative stain data collection and processing

Purified Exo70-I114F exocyst was negatively stained with uranyl formate and imaged using a Talos-Arctica (FEI) at 200 V equipped with a K3 direct electron detector (Gatan) operating in superresolution mode. Using SerialEM, 5,424 micrographs were taken at 45,000× with a pixel size of 0.435 Å and a target defocus of −0.2 to −2 µm. A video of 36 frames was taken for each micrograph, and motion correction was performed using the Align Frames module in IMOD with 2× binning, resulting in a final pixel size of 0.917 Å (Mastronarde, 2017). The I114F exocyst dataset was processed using the cisTEM software package (Grant et al., 2018). Briefly, CTF values were estimated using CTFfind (Mindell and Grigorieff, 2003; Rohou and Grigorieff, 2015), and two rounds of 2D classification (50 classes and 20

iterations) were used to select particles, yielding a total of 122,636 particles for 3D reconstruction. An ab initio model was generated from this particle stack (Grigorieff 2016). Four 3D classes were generated from this model and further refined and finally sharpened in cisTEM using the ab initio model low-pass filtered to 20 Å as a mask. The Fourier shell correlation (FSC) curve and angular distribution plot of the final reconstruction are shown in Fig. S4.

The 3D reconstruction of the wild-type exocyst used a previously collected dataset of Sec15-GFP complex described in Heider et al. (2016). Briefly, micrographs were collected using a Titan Krios electron microscope operated at 300 kV with 29,000× nominal magnification. The defocus values ranged from 0.5 to 3.0 µm, and images were automatically taken with EPU software (FEI) with a final pixel size of 2.81 Å. CTF values were estimated using GCTF v1.06 (Zhang 2016). This dataset was processed in cryoSPARC v2.9.0 (Punjani et al., 2017), and 2D refinement used to filter the particle set to 67,509 particles for 3D classification. After 3D classification, 51,685 particles were selected for "gold standard" homogeneous refinement to yield an estimated 15-Å 3D map (Fig. S4). This unsharpened map was then low-pass filtered to the nominal size of the uranyl acetate grain size of ∼15 Å and is shown in Fig. 3. The angular distribution plot for the wild-type 3D reconstruction is shown in Fig. S4. The UCSF Chimera package was used to generate the molecular graphics (Pettersen et al., 2004).

Online supplemental material

Fig. S1 shows negative stain micrographs of Exo70-114 exocyst complexes along with 2D averages. Fig. S2 shows a comparison of 2D averages for wild-type, Exo70-I114F, and Exo70-G388R exocyst complexes. Fig. S3 uses gold-labeling specific to the Exo70 subunit, to demonstrate that both wild-type Exo70 and Exo70-I114F remain associated with the exocyst complex during negative stain EM. Fig. S4 shows the FSC curves and angular distribution plots for the wild-type Exo70 and Exo70-I114F 3D negative stain models shown in Fig. 3.

Acknowledgments

We thank W. Kennedy for technical assistance, P. Thomas and M. Harrington for computational support, H. Meekel for negative stain EM analysis of tethering reactions, D. Lew (Duke University) for the gift of *boi1-11* strain, and B. Miller for critical reading of the manuscript. Also, a special thanks to Dr. Chen Xu and the University of Massachusetts cryo-EM facility for their assistance in single-particle data collection, as well as members of the Kelch laboratory (University of Massachusetts Medical School) for their assistance and advice in processing with *cis*TEM.

Work in our laboratories is supported by National Institutes of Health grants GM054712 (P. Brennwald), T32GM119999 (M. Plooster), F31MH116576 (M. Plooster), GM068803 (M. Munson), F32GM123704 (D. Lepore), GM127673 (A. Frost), and DP2GM110772 (A. Frost). A. Frost is an American Asthma Foundation Scholar, a Howard Hughes Medical Institute Faculty Scholar, and a Chan Zuckerberg Biohub Investigator. L. Kenner was supported by a graduate research fellowship from the National Science Foundation. The University of California San Francisco Center for Advanced Cryo-EM is partially supported in part by National Institutes of Health grants S10OD020054, 1S10OD021741, and 1S10OD026881-01 and the Howard Hughes Medical Institute. UCSF Chimera is developed by the Resource for Biocomputing, Visualization, and Informatics and supported by the National Institute of General Medical Sciences P41-GM103311 (Pettersen et al., 2004).

The authors declare no competing financial interests.

Author contributions: G. Rossi performed the studies shown in Figs. 1, 2, 4, and 5. D. Lepore performed the studies shown in Figs. 3, 6, S1, S2, S3, and S4. L. Kenner performed the studies shown in Fig. S2. A.B. Czuchra performed the studies shown in Fig. S3. M. Plooster performed the work in Fig. 2 A. G. Rossi and P. Brennwald wrote the first draft, with M. Munson, A. Frost, D. Lepore contributing sections related to negative stain EM and 3D reconstruction modeling. The final paper was edited by G. Rossi, D. Lepore, A. Frost, M. Munson, and P. Brennwald.

Submitted: 25 April 2019
Revised: 26 July 2019
Accepted: 19 November 2019

References

Adamo, J.E., J.J. Moskow, A.S. Gladfelter, D. Viterbo, D.J. Lew, and P.J. Brennwald. 2001. Yeast Cdc42 functions at a late step in exocytosis, specifically during polarized growth of the emerging bud. *J. Cell Biol.* 155:581–592. https://doi.org/10.1083/jcb.200106065

Adamo, J.E., G. Rossi, and P. Brennwald. 1999. The Rho GTPase Rho3 has a direct role in exocytosis that is distinct from its role in actin polarity. *Mol. Biol. Cell.* 10:4121–4133. https://doi.org/10.1091/mbc.10.12.4121

Baker, R.W., and F.M. Hughson. 2016. Chaperoning SNARE assembly and disassembly. *Nat. Rev. Mol. Cell Biol.* 17:465–479. https://doi.org/10.1038/nrm.2016.65

Boyd, C., T. Hughes, M. Pypaert, and P. Novick. 2004. Vesicles carry most exocyst subunits to exocytic sites marked by the remaining two subunits, Sec3p and Exo70p. *J. Cell Biol.* 167:889–901. https://doi.org/10.1083/jcb.200408124

Croteau, N.J., M.L. Furgason, D. Devos, and M. Munson. 2009. Conservation of helical bundle structure between the exocyst subunits. *PLoS One.* 4: e4443. https://doi.org/10.1371/journal.pone.0004443

Dong, G., A.H. Hutagalung, C. Fu, P. Novick, and K.M. Reinisch. 2005. The structures of exocyst subunit Exo70p and the Exo84p C-terminal domains reveal a common motif. *Nat. Struct. Mol. Biol.* 12:1094–1100. https://doi.org/10.1038/nsmb1017

Dubuke, M.L., S. Maniatis, S.A. Shaffer, and M. Munson. 2015. The exocyst subunit Sec6 interacts with assembled exocytic SNARE complexes. *J. Biol. Chem.* 290:28245–28256. https://doi.org/10.1074/jbc.M115.673806

Finger, F.P., T.E. Hughes, and P. Novick. 1998. Sec3p is a spatial landmark for polarized secretion in budding yeast. *Cell.* 92:559–571. https://doi.org/10.1016/S0092-8674(00)80948-4

Grant, T., A. Rohou, and N. Grigorieff. 2018. *cis*TEM, user-friendly software for single-particle image processing. *eLife.* 7:e35383. https://doi.org/10.7554/eLife.35383

Grigorieff, N. 2016. Frealign: An exploratory tool for single-particle cryo-EM. *Methods Enzymol.* 579:191–226. https://doi.org/10.1016/bs.mie.2016.04.013

Grosshans, B.L., D. Ortiz, and P. Novick. 2006. Rabs and their effectors: achieving specificity in membrane traffic. *Proc. Natl. Acad. Sci. USA.* 103: 11821–11827. https://doi.org/10.1073/pnas.0601617103

Guo, W., A. Grant, and P. Novick. 1999b. Exo84p is an exocyst protein essential for secretion. *J. Biol. Chem.* 274:23558–23564. https://doi.org/10.1074/jbc.274.33.23558

Guo, W., D. Roth, C. Walch-Solimena, and P. Novick. 1999a. The exocyst is an effector for Sec4p, targeting secretory vesicles to sites of exocytosis. *EMBO J.* 18:1071–1080. https://doi.org/10.1093/emboj/18.4.1071

Guo, W., F. Tamanoi, and P. Novick. 2001. Spatial regulation of the exocyst complex by Rho1 GTPase. *Nat. Cell Biol.* 3:353–360. https://doi.org/10.1038/35070029

Hakhverdyan, Z., M. Domanski, L.E. Hough, A.A. Oroskar, A.R. Oroskar, S. Keegan, D.J. Dilworth, K.R. Molloy, V. Sherman, J.D. Aitchison, et al. 2015. Rapid, optimized interactomic screening. *Nat. Methods.* 12: 553–560. https://doi.org/10.1038/nmeth.3395

Harms, F.L., K. Kloth, A. Bley, J. Denecke, R. Santer, D. Lessel, M. Hempel, and K. Kutsche. 2018. Activating mutations in PAK1, encoding p21-activated kinase 1, cause a neurodevelopmental disorder. *Am. J. Hum. Genet.* 103: 579–591. https://doi.org/10.1016/j.ajhg.2018.09.005

Hattendorf, D.A., A. Andreeva, A. Gangar, P.J. Brennwald, and W.I. Weis. 2007. Structure of the yeast polarity protein Sro7 reveals a SNARE regulatory mechanism. *Nature.* 446:567–571. https://doi.org/10.1038/nature05635

He, B., F. Xi, X. Zhang, J. Zhang, and W. Guo. 2007. Exo70 interacts with phospholipids and mediates the targeting of the exocyst to the plasma membrane. *EMBO J.* 26:4053–4065. https://doi.org/10.1038/sj.emboj.7601834

Heider, M.R., M. Gu, C.M. Duffy, A.M. Mirza, L.L. Marcotte, A.C. Walls, N. Farrall, Z. Hakhverdyan, M.C. Field, M.P. Rout, et al. 2016. Subunit connectivity, assembly determinants and architecture of the yeast exocyst complex. *Nat. Struct. Mol. Biol.* 23:59–66. https://doi.org/10.1038/nsmb.3146

Inoue, M., L. Chang, J. Hwang, S.H. Chiang, and A.R. Saltiel. 2003. The exocyst complex is required for targeting of Glut4 to the plasma membrane by insulin. *Nature.* 422:629–633. https://doi.org/10.1038/nature01533

Jahn, R., and D. Fasshauer. 2012. Molecular machines governing exocytosis of synaptic vesicles. *Nature.* 490:201–207. https://doi.org/10.1038/nature11320

Kustermann, J., Y. Wu, L. Rieger, D. Dedden, T. Phan, P. Walther, A. Dünkler, and N. Johnsson. 2017. The cell polarity proteins Boi1p and Boi2p stimulate vesicle fusion at the plasma membrane of yeast cells. *J. Cell Sci.* 130:2996–3008. https://doi.org/10.1242/jcs.206334

Lehman, K., G. Rossi, J.E. Adamo, and P. Brennwald. 1999. Yeast homologues of tomosyn and lethal giant larvae function in exocytosis and are associated with the plasma membrane SNARE, Sec9. *J. Cell Biol.* 146: 125–140.

Lepore, D.M., L. Martínez-Núñez, and M. Munson. 2018. Exposing the elusive exocyst structure. *Trends Biochem. Sci.* 43:714–725. https://doi.org/10.1016/j.tibs.2018.06.012

Masgrau, A., A. Battola, T. Sanmartin, L.P. Pryszcz, T. Gabaldón, and M. Mendoza. 2017. Distinct roles of the polarity factors Boi1 and Boi2 in the control of exocytosis and abscission in budding yeast. *Mol. Biol. Cell.* 28: 3082–3094. https://doi.org/10.1091/mbc.e17-06-0404

Mastronarde, D. 2017. Alignframes (1). General commands manual. Available at: https://bio3d.colorado.edu/imod/betaDoc/man/alignframes.html (accessed September 9, 2019).

Mei, K., Y. Li, S. Wang, G. Shao, J. Wang, Y. Ding, G. Luo, P. Yue, J.J. Liu, X. Wang, et al. 2018. Cryo-EM structure of the exocyst complex. *Nat. Struct. Mol. Biol.* 25:139–146. https://doi.org/10.1038/s41594-017-0016-2

Mindell, J.A., and N. Grigorieff. 2003. Accurate determination of local defocus and specimen tilt in electron microscopy. *J. Struct. Biol.* 142:334–347. https://doi.org/10.1016/S1047-8477(03)00069-8

Morgera, F., M.R. Sallah, M.L. Dubuke, P. Gandhi, D.N. Brewer, C.M. Carr, and M. Munson. 2012. Regulation of exocytosis by the exocyst subunit Sec6 and the SM protein Sec1. *Mol. Biol. Cell.* 23:337–346. https://doi.org/10.1091/mbc.e11-08-0670

Munson, M., and P. Novick. 2006. The exocyst defrocked, a framework of rods revealed. *Nat. Struct. Mol. Biol.* 13:577–581. https://doi.org/10.1038/nsmb1097

Nejsum, L.N., and W.J. Nelson. 2009. Epithelial cell surface polarity: the early steps. *Front. Biosci.* 14:1088–1098. https://doi.org/10.2741/3295

Oeffinger, M., K.E. Wei, R. Rogers, J.A. DeGrasse, B.T. Chait, J.D. Aitchison, and M.P. Rout. 2007. Comprehensive analysis of diverse ribonucleoprotein complexes. *Nat. Methods.* 4:951–956. https://doi.org/10.1038/nmeth1101

Otomo, T., C. Otomo, D.R. Tomchick, M. Machius, and M.K. Rosen. 2005. Structural basis of Rho GTPase-mediated activation of the formin mDia1. *Mol. Cell.* 18:273–281. https://doi.org/10.1016/j.molcel.2005.04.002

Pathak, R., and C. Dermardirossian. 2013. GEF-H1: orchestrating the interplay between cytoskeleton and vesicle trafficking. *Small GTPases.* 4:174–179. https://doi.org/10.4161/sgtp.24616

Pettersen, E.F., T.D. Goddard, C.C. Huang, G.S. Couch, D.M. Greenblatt, E.C. Meng, and T.E. Ferrin. 2004. UCSF Chimera--a visualization system for exploratory research and analysis. *J. Comput. Chem.* 25:1605–1612. https://doi.org/10.1002/jcc.20084

Polgar, N., and B. Fogelgren. 2018. Regulation of Cell Polarity by Exocyst-Mediated Trafficking. *Cold Spring Harb. Perspect. Biol.* 10:a031401. https://doi.org/10.1101/cshperspect.a031401

Punjani, A., J.L. Rubinstein, D.J. Fleet, and M.A. Brubaker. 2017. cryoSPARC: algorithms for rapid unsupervised cryo-EM structure determination. *Nat. Methods.* 14:290–296. https://doi.org/10.1038/nmeth.4169

Rohou, A., and N. Grigorieff. 2015. CTFFIND4: Fast and accurate defocus estimation from electron micrographs. *J. Struct. Biol.* 192:216–221. https://doi.org/10.1016/j.jsb.2015.08.008

Rossi, G., K. Watson, M. Demonch, B. Temple, and P. Brennwald. 2015. *In vitro* reconstitution of Rab GTPase-dependent vesicle clustering by the yeast lethal giant larvae/tomosyn homolog, Sro7. *J. Biol. Chem.* 290:612–624. https://doi.org/10.1074/jbc.M114.595892

Rossi, G., K. Watson, W. Kennedy, and P. Brennwald. 2018. The tomosyn homologue, Sro7, is a direct effector of the Rab GTPase, Sec4, in post-Golgi vesicle tethering. *Mol. Biol. Cell.* 29:1476–1486. https://doi.org/10.1091/mbc.E18-02-0138

Roumanie, O., H. Wu, J.N. Molk, G. Rossi, K. Bloom, and P. Brennwald. 2005. Rho GTPase regulation of exocytosis in yeast is independent of GTP hydrolysis and polarization of the exocyst complex. *J. Cell Biol.* 170: 583–594. https://doi.org/10.1083/jcb.200504108

Shen, D., H. Yuan, A. Hutagalung, A. Verma, D. Kümmel, X. Wu, K. Reinisch, J.A. McNew, and P. Novick. 2013. The synaptobrevin homologue Snc2p recruits the exocyst to secretory vesicles by binding to Sec6p. *J. Cell Biol.* 202:509–526. https://doi.org/10.1083/jcb.201211148

TerBush, D.R., T. Maurice, D. Roth, and P. Novick. 1996. The Exocyst is a multiprotein complex required for exocytosis in Saccharomyces cerevisiae. *EMBO J.* 15:6483–6494. https://doi.org/10.1002/j.1460-2075.1996.tb01039.x

Watson, K., G. Rossi, B. Temple, and P. Brennwald. 2015. Structural basis for recognition of the Sec4 Rab GTPase by its effector, the Lgl/tomosyn homologue, Sro7. *Mol. Biol. Cell.* 26:3289–3300. https://doi.org/10.1091/mbc.e15-04-0228

Wu, H., and P. Brennwald. 2010. The function of two Rho family GTPases is determined by distinct patterns of cell surface localization. *Mol. Cell. Biol.* 30:5207–5217. https://doi.org/10.1128/MCB.00366-10

Wu, H., G. Rossi, and P. Brennwald. 2008. The ghost in the machine: small GTPases as spatial regulators of exocytosis. *Trends Cell Biol.* 18:397–404. https://doi.org/10.1016/j.tcb.2008.06.007

Wu, H., C. Turner, J. Gardner, B. Temple, and P. Brennwald. 2010. The Exo70 subunit of the exocyst is an effector for both Cdc42 and Rho3 function in polarized exocytosis. *Mol. Biol. Cell.* 21:430–442. https://doi.org/10.1091/mbc.e09-06-0501

Yue, P., Y. Zhang, K. Mei, S. Wang, J. Lesigang, Y. Zhu, G. Dong, and W. Guo. 2017. Sec3 promotes the initial binary t-SNARE complex assembly and membrane fusion. *Nat. Commun.* 8:14236. https://doi.org/10.1038/ncomms14236

Zhang, K. 2016. Gctf: Real-time CTF determination and correction. *J. Struct. Biol.* 193:1–12. https://doi.org/10.1016/j.jsb.2015.11.003

Zhang, X., E. Bi, P. Novick, L. Du, K.G. Kozminski, J.H. Lipschutz, and W. Guo. 2001. Cdc42 interacts with the exocyst and regulates polarized secretion. *J. Biol. Chem.* 276:46745–46750. https://doi.org/10.1074/jbc.M107464200

Zhang, X., K. Orlando, B. He, F. Xi, J. Zhang, A. Zajac, and W. Guo. 2008. Membrane association and functional regulation of Sec3 by phospholipids and Cdc42. *J. Cell Biol.* 180:145–158. https://doi.org/10.1083/jcb.200704128

Zhang, X., P. Wang, A. Gangar, J. Zhang, P. Brennwald, D. TerBush, and W. Guo. 2005. Lethal giant larvae proteins interact with the exocyst complex and are involved in polarized exocytosis. *J. Cell Biol.* 170: 273–283. https://doi.org/10.1083/jcb.200502055